



Erdem, E. and Kontis, K. (2021) Experimental investigation of sonic transverse jets in Mach 5 crossflow. *Aerospace Science and Technology*, 110, 106419.

(doi: [10.1016/j.ast.2020.106419](https://doi.org/10.1016/j.ast.2020.106419))

This is the Author Accepted Manuscript.

There may be differences between this version and the published version. You are advised to consult the publisher's version if you wish to cite from it.

<https://eprints.gla.ac.uk/226959/>

Deposited on: 7 December 2020

# Experimental Investigation of Sonic Transverse Jets in Mach 5 Crossflow

Erinc Erdem<sup>1</sup>, Konstantinos Kontis<sup>2</sup>

*School of Engineering, James Watt South Building, Glasgow G12 8QQ, UK*

---

## Abstract

An experimental investigation of sonic transverse jets in Mach 5 cross flow over a flat plate with a sharp leading edge was carried out. Jet to free stream momentum flux ratio,  $J$ , was varied from 1.16 to 5.30. Schlieren visualisation provided information regarding mean flow features such as Mach disc height,  $h$ , separation length,  $x_{sep}$  as well as inherent unsteadiness. Steady wall pressure measurements diagnosed the interaction region between the jet and the incoming cross flow developing on the flat plate. To assess the jet penetration characteristics and trajectories, two-component Particle Image Velocimetry (PIV) measurements were carried out at the centreplane of the flat plate. Raw PIV image analysis was used to specify jet penetration boundaries. Ensemble-averaged streamwise and transverse velocity contours revealed the mean flow structures. The barrel shocks and the Mach disc forming the jet boundary can be easily seen and were visualised/quantified using PIV measurement technique. Maximum turbulence occurred above the Mach disc due to the presence of the shear layer and at the intersection of the windward side of the barrel shock and bow shock.

*Keywords:* Jets, Compressible Flow, PIV,

---

---

<sup>1</sup>erincerdem@gmail.com, Visiting Research Associate

<sup>2</sup>kostas.kontis@glasgow.ac.uk, Professor of Aerospace Engineering

## Nomenclature

$C_d$	Discharge coefficient for jet orifice
$d$	Diameter, m
$h$	Jet penetration height, m
$Kn$	Knudsen number
$J$	Momentum flux ratio
$M$	Mach number
$\dot{m}$	Mass flow rate, kg/s
$p$	Pressure, mbar
$Re$	Reynolds number
$Re/m$	Unit Reynolds number, 1/m
$Sk$	Stokes number
$SR$	Spatial ratio for PIV
$T$	Temperature, K
$t$	Time, sec
$TR$	Temporal ratio for PIV
$u, v$	streamwise and transverse velocity components, m/s
$V$	Velocity, m/s
$\gamma$	Ratio of specific heats
$\mu$	Viscosity, Pa.sec
$\rho$	Density, kg/m <sup>3</sup>
$\tau$	Time scale, sec
$\xi$	Relaxation distance for PIV, m

### *Subscript*

$D$	Based on diameter
$f$	Flow
$jet$	Jet
$p$	Particle
$pitot$	Pitot
$theo$	Theoretical

$v$	Based on slip velocity
0	Stagnation condition
$\infty$	Free stream
<i>Superscript</i>	
'	Fluctuation

## 1. Introduction

Transverse jet injection into supersonic/hypersonic crossflows finds its use on many engineering applications such as scramjet combustors, thrust vector  
5 control systems and reaction control jets. The interaction of the transverse jet with the high speed cross flow creates complex three dimensional flow patterns that are abound with shock waves, separations regions, shear layers and wakes so on. The resultant flowfield has received significant interest since the 1960's. Earlier studies were focused on wind tunnel experiments utilising conventional  
10 measurement techniques such as schlieren/shadowgraph photography, wall pressure and concentration measurements to gain a better understanding of the jet interaction and penetration phenomena[1]-[7]. These studies examined the effect of the injection pressure ratio, the location of injection and the state of the incoming boundary layer and lastly the type of injectant gas. Furthermore  
15 several other studies investigated the mixing performance and penetration characteristics of transverse jets in high speed cross flows at relatively low supersonic Mach numbers in "cold" wind tunnels [8]-[9]. These studies provided valuable experimental data shedding light on jet penetration and relevant jet trajectories measured by Mie and Rayleigh scattering methods. Specifically, Ben-Yakar  
20 [10] investigated convection and mixing characteristics of hydrogen and ethylene transverse jets at Mach 3.4, in an expansion tube with realistic upstream conditions for scramjet applications. Ultra high speed schlieren photography and Planar Laser Induced Fluorescence (PLIF) of OH radicals were utilised to obtain detailed information on the molecular mixing. This study was very valu-



25 able in terms of understanding the mechanism behind mixing; and it was found  
 to be the promotion of small scale structures rather than global manipulations  
 of main stream as chemical reactions occur at molecular level. The near field  
 mixing of transverse jets is dominated by the so called “entrainment-stretching-  
 mixing process” [10] driven by large scale jet shear layer vortices as they are  
 30 shown in Fig. 1 (top figure). Due to the obstruction introduced by transverse  
 jet, a bow shock forms and stands off from injector orifice. In the region between  
 the bow shock and the transverse jet, the injectant fluid moves with a higher  
 velocity tangentially to the interface than the free stream fluid. As a result,  
 large vortices are periodically formed engulfing large quantities of free stream  
 35 fluid and drawing it into the jet shear layer (macro-mixing). These vortices  
 are convected downstream at high speeds, where the injectant and air are then  
 mixed by slow molecular diffusion due to Kelvin-Helmholtz instabilities [11]. In  
 general, large scale structures are beneficial for the enhancement of bulk mixing,  
 but they hinder fine scale or molecular mixing. However, they also stretch the  
 40 interface between unmixed fluids. Stretching increases the interfacial area and  
 simultaneously steepens the local concentration gradients along the entire sur-  
 face while enhancing the diffusive micro mixing [10]. In terms of other coherent  
 structures, horseshoe vortices formed by the upstream separated regions due to  
 the adverse pressure gradient caused by the bow shock, wrap around the jet  
 45 periphery and convect downstream as they are shown in Fig. 1 (bottom figure).  
 Counter rotating vortices develop on top of the normal shock (Mach disc) that  
 is caused by sudden expansion of the jet stream. These counter rotating cross  
 flow vortices are assessed by Santiago and Dutton [12] as the primary source  
 of entrainment of surrounding incoming flow air into the injectant’s flow that  
 50 is important for farfield mixing. They are produced by folding of the vortex  
 ring, which is the downstream manifestation of vorticity arising from the injec-  
 tors sidewall boundary layers [13]. Finally, wake vortices periodically shed near  
 the base of the inner jet core and trail downstream under the jet plume [12],  
 [14]. Perurena et al.[15] examined water injection in a Mach 6 cross flow and  
 55 extracted data regarding penetration height, lateral extension, mixing and ve-

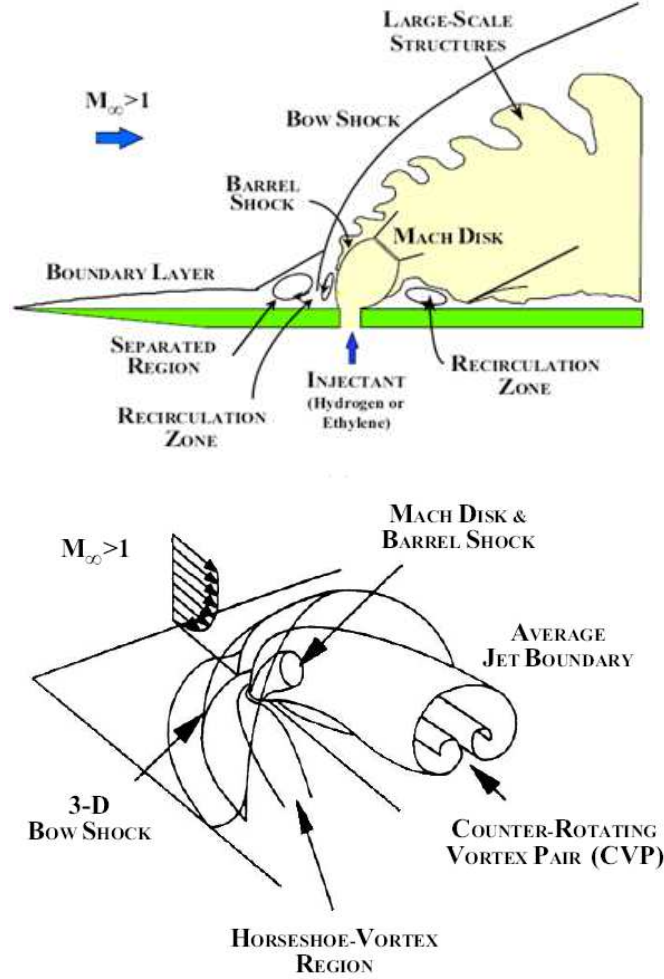


Figure 1: Top: mixing features of an underexpanded transverse injection into a supersonic cross flow by BenYakar [10]; bottom: three dimensional perspective of the averaged features of the flowfield by Gruber [8].

locity of the injected jet using high speed schlieren photography and front/back lighted illumination. High speed shadowgraph/schlieren photography identified the unsteady flow structures such as the bow shock or separation shock and their respective frequencies. The correlations were proposed relating jet penetration  
 60 height and lateral extension with the injection ratio and orifice diameter for

circular injector jets. The mixing of the jet with the crossflow was completed at a distance of around 40 jet diameters, independent of the effects of momentum flux ratio,  $J$ , which is defined below in Eqn. 1.

$$J = \frac{\gamma_{jet} p_{jet} M_{jet}^2}{\gamma_{\infty} p_{\infty} M_{\infty}^2} \quad (1)$$

where  $\gamma$  is the specific heat ratio,  $p$  is the pressure,  $M$  is the Mach number  
65 and subscripts  $\infty$  and  $jet$  refer to freestream and jet conditions.

A study by Erdem et. al [16] shed light on the mixing characteristics of jets of different gases such as air, carbon dioxide and helium at Mach 5 cross flow. Although the momentum flux ratio of different gases was kept the same, their penetration and mixing characteristics were dissimilar both in the jet nearfield  
70 and farfield. Schlieren photography together with two-dimensional Particle Image Velocimetry (PIV) were utilised as flow diagnostic tools. First time in open literature, velocity components and related turbulence intensities were quantified and some of the coherent structures were visualised with PIV measurements. Capable of providing instantaneous planar velocity fields, PIV has been success-  
75 fully applied to high Mach number flows in the last decade by Haertig et al. [17] and Schrijer et al. [18].

The extension of PIV to high Mach number regime involves certain challenges such as selection and uniform seeding of appropriate solid particles, the examination of the particle time response and the analysis of particle image  
80 recordings where a large variation in particle image density occurs due to shock waves [19].

Huang [20] compiled recent studies in this field in detail. Also recent studies from Huh and Lee [21], Zhao et al. [22], Williams et al. [30], Liu et al. [24] numerically investigated the interaction of the jets with supersonic cross flow  
85 using high fidelity numerical methods. In addition various authors examined jets in supersonic cross flow in a scramjet engine, numerically [27], [28], [29], [30]. Specifically Miller et al. [25] numerically investigated transient interaction between a reaction control jet and Mach 5 cross flow using data from the thesis

of Erdem [26]. The aim was to understand the mechanism of side force gener-  
 90 ation due to surface pressure distribution using Large Eddy Simulation (LES).  
 Pertinent flow structures have been captured by LES and discussed in detail.  
 The present study stems from this thesis and constitutes a challenging appli-  
 cation of PIV to investigate sonic transverse air jet in Mach 5 cross flow with  
 varying momentum flux ratio inside a blowdown wind tunnel. It aims to pro-  
 95 vide good quality reliable experimental data in terms of velocity and turbulence  
 fields, jet mixing and penetration characteristics with changing momentum flux  
 ratio, which is the continuation of authors previous study [16]. Wall pressure  
 measurements and schlieren visualisation are also conducted to provide a solid  
 foundation in terms of steady wall pressures and oscillating flow features.

## 100 2. Experimental Setup

The details of the experimental facility, test model and the associated mea-  
 surement techniques were elaborated in Refs. [16], [26], [31], [32]. They are  
 briefly mentioned in following subsections.

### *2.1. University of Manchester HSST*

105 The experiments are conducted in the High Supersonic Tunnel (HSST) at the  
 University of Manchester. The tunnel is an intermediate blowdown (pressure-  
 vacuum) type which uses dry air as working fluid. The tunnel uses a contoured  
 axisymmetric Mach 5 nozzle immediately downstream of the settling chamber.  
 The stagnation pressure can range from 5 to 8 bar and thereby unit Reynolds  
 110 numbers,  $\text{Re}/m$ , of between  $4 - 16 \cdot 10^6/m$  can be achieved [31] - [32]. The  
 tunnel working section is an enclosed free jet design. The calibration of the  
 facility was carried out by the authors; the variations in Mach number and unit  
 Reynolds number were found to be  $\pm 0.4\%$  and  $\pm 3.7\%$  respectively. The useful  
 running time is found to be 7.5 seconds. Stagnation pressure  $p_0$ , and stagnation  
 115 temperature,  $T_0$ , measurements are done using a Pitot probe attached to an  
 absolute pressure transducer, Kulite XTE-190M (6.89 bar range), and a K-  
 type thermocouple probe at the settling chamber. Analogue signals from the

sensors are acquired by a high speed Data Acquisition (DAQ) card, National Instruments (NI) PCI-6251, after they are conditioned by a SCXI-1000 unit.

## 120 2.2. Schlieren visualisation

Toepler's z-type schlieren technique, adapted for flow visualisation, consists of a continuous light source of Palflash 501 (Pulse Photonics) with a focusing lens and a 1 mm wide slit, two 203.2 mm parabolic mirrors with 1828.8 mm focal length, a knife edge, a set of Hoya 49 mm close-up lenses and a digital Canon  
125 SLR camera, EOS-450D, 12MP. The camera is set to continuous recording mode at 3.5 fps with full resolution; the shutter speed is adjusted to maximum value of 1/4000 sec with an ISO speed of 400 to provide enough detail and appropriate brightness. The digital resolution is approximately 34 pixels per mm. In addition a high speed Photron SA-1 High Speed Video system is utilised to record  
130 time-resolved Schlieren images up to 675000 fps at various pixel resolutions and shutter speeds. The optimum frame rate is based on a compromise between adequate temporal resolution and pixel resolution. 1  $\mu$ sec at 16000 fps to resolve flow features with sharpness. The digital resolution is approximately 10 pixels per mm. The layout of the optical setup and the data acquisition architecture  
135 with measurement chain is shown in Fig. 2.

## 2.3. Test model

The model used for this study is a sharp leading edged flat plate (leading edge thickness smaller than 100  $\mu$ m) with a converging circular jet orifice of 2.2 mm in diameter, through which a sonic turbulent jet of air is injected after  
140 regulation. The flat plate is 155 mm long, 68 mm wide and 5 mm thick and painted matt black to avoid reflections for PIV application. The jet orifice is located at 105 mm from the leading edge at the centreline. The jet stagnation pressure,  $p_{0jet}$ , is adjusted with the help of a pressure transducer, Kulite XTE-190M (3.5bar range) that is connected to an 8 mm air pipe via T-junction. In  
145 case of wall pressure measurements, a housing for pressure transducers is used and 1mm tappings on model are connected to this housing via flexible heat

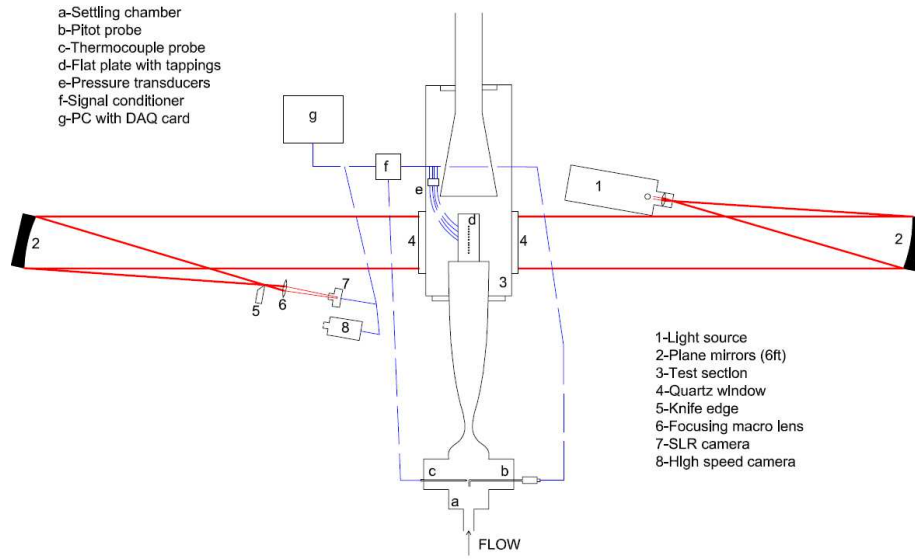


Figure 2: Schematic setup of Schlieren visualisation with data acquisition architecture [31],[32].

resistant tubing with pressure transducers, Kulite XTE-190M (0.7 bar range), being connected to the other side of the housing. The model, situated inside the test section, is shown in Fig. 3.

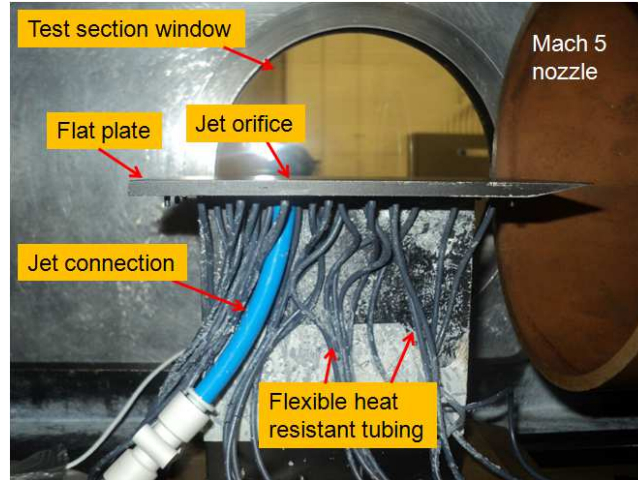


Figure 3: Flat plate model placed inside test section.

## 150 2.4. Wall pressure measurements

In terms of non dimensional surface pressure values, the data reduction procedure for surface pressure measurements is as follows;  $p_\infty(t)$  is calculated using isentropic relations from  $p_0(t)$ , i.e.  $(= p_0 / (1 + (\gamma - 1)/2 M_\infty^2)^{\gamma/(\gamma-1)})$ . Then the divided signals of  $p_w(t)/p_\infty(t)$  and  $p_{0jet}(t)/p_\infty(t)$  signals are obtained. 155 These signals are integrated and averaged over the duration of the stagnation pressure plateau of a test run.

$$\begin{aligned}\overline{p_w/p_\infty} &= \frac{1}{t_f - t_i} \int_{t_i}^{t_f} p_w(t)/p_\infty(t) dt \\ \overline{p_{0jet}/p_\infty} &= \frac{1}{t_f - t_i} \int_{t_i}^{t_f} p_{0jet}(t)/p_\infty(t) dt\end{aligned}\quad (2)$$

## 2.5. PIV measurement technique

Two component PIV measurements are carried out on the centreline of the model with a dedicated PIV system, which includes a seeding device that dis- 160 charge particles through the jet orifice, an illuminating laser with related optics to create a laser sheet and a recording camera. The following subsections describe the subsystems briefly; these can also be found in Refs. [16], [26].

### 2.5.1. Seeding

The particles seeded into flow field through the jet orifice, enable to visualize 165 and then to extract the velocity information of the fluid motion. Aluminium oxide powder particles (dehydrated prior to experiments) with a nominal crystal size of 300 nm are used with a nominal bulk density of  $\rho_p = 3970 \text{ kg/m}^3$ . A PS-10 powder seeder device from Dantec Dynamics, is used to generate an airflow seeded with particles.

170 The flow tracing capability of particles of diameter,  $d_p$ , and a particle density,  $\rho_p$ , with a fluid viscosity,  $\mu_f$ , is usually quantified through the particle relaxation time,  $\tau_p$ . The theoretical behavior for small spherical particles may be reduced to the modified Stokes drag law defined by Melling [33]. Given the relatively low value of the Mach number and Reynolds number based on the particle diameter,

175 the modified drag relation that takes into account rarefaction effects yields the  
 expression for the relaxation time in Eqn. 3, where  $Kn_d$  is the Knudsen number  
 based on the particle diameter, which is defined in Eqn. 4.  $Re_d$  is the Reynolds  
 number based on the diameter of the particle and  $M_v$  is the Mach number both  
 evaluated for the maximum particle slip velocity  $\Delta V$  [19].

$$\tau_p = \frac{\rho_p d_p^2 (1 + 2.7Kn_d)}{18\mu_f} \quad (3)$$

180 where

$$Kn_d = 1.26\sqrt{\gamma} (M_v/Re_d) \quad (4)$$

As suggested by Samimy and Lele [34], particle dynamic effects may be fur-  
 ther quantified by the Stokes number,  $Sk$ , written in Eqn. 5. For accurate flow  
 tracking the time scale of the flow has to be greater than the time response of  
 the particles, i.e.  $Sk \ll 1$ . The characteristic flow time scale is found to be  
 185 70  $\mu sec$  by assuming  $\Delta V$  as  $U_{jet}$  (jet velocity) and  $\delta$  (shear layer thickness)  
 as  $d_{jet}$  (jet diameter) as it is shown in Eqn. 5; whereas the particle time re-  
 sponse is calculated to be 3-1.6  $\mu sec$  respectively using sonic air jet conditions  
 ( $T_{0jet} = 295K, p_{0jet} = 685mbar - 3040mbar, U_{jet} = 315m/s$ ) specified in Table  
 2. Therefore, theoretical value of the Stokes number is found to be in the range  
 190 of 0.04-0.02 for the tests 1-3, as it is shown in Table 1 respectively, indicating  
 that the particles follow the flow with fidelity.

$$Sk = \frac{\tau_p}{\tau_f} \quad \text{where} \quad \tau_f = 10 \frac{\delta}{\Delta V} \approx 10 \frac{d_{jet}}{U_{jet}} \quad (5)$$

Table 1: Particle tracking characteristics for tests 1-3.

Test	$U_{jet}$	$M_v$	$Re_d$	$Kn_d$	$\tau_p$	$\tau_f$	Sk
No	(m/s)				$\mu sec$	$\mu sec$	
1	315	1	2.97	0.50	2.95	70	0.04
2	315	1	7.08	0.21	1.97	70	0.03
3	315	1	13.57	0.11	1.63	70	0.02



### 2.5.2. Illumination

A Litron Nano L series, Nd:Yag Q-switched laser is used for PIV illumination. The laser has the pulse energy of 200 mJ at repetition rate of 15 Hz. The  
195 laser beams are pulsed at the wavelength of 532 nm. The pulse width of the light  
is 6 ns and the pulse separation time (the time interval between two consecutive  
PIV images light pulses,  $\Delta t$ ) can be adjusted to 0.1  $\mu$ sec as minimum. A laser  
sheet of 0.5 mm thickness is produced with a series of spherical and cylindrical  
lenses and directed above the test section via a laser guide arm.

### 2.5.3. Image Recording

A LaVision Imager ProX2M CCD camera with  $1600 \times 1200 \text{ pixel}^2$  resolution  
(with 7.4  $\mu\text{m}$  pixel pitch) is used to record scattered light reflecting from parti-  
cles at 14 bit digitisation. The camera is equipped with a Sigma 105 mm focal  
objective lens with  $f$  number of 5.6, in combination with a narrow-bandpass  
205 532 nm filter in order to minimize ambient light interference.

### 2.5.4. Setup

The PIV setup is arranged such that it can produce a laser sheet that is  
tilted at 45 degrees with respect to the flat plate due to access restrictions, as  
it is shown in Fig. 4. The laser sheet is localised at the centreplane where the  
210 flow field can be assumed symmetrical with respect to the centreplane. Owing  
to the angled arrangement of the laser sheet the reflection of laser light from  
the mat black flat plate surface is reduced around the jet orifice. Laser sheet  
thickness of 0.5 mm compared to 2.2 mm jet diameter introduce some effects  
of unavoidable out of plane motion into measurements. In the tests, only the  
215 transverse jet is seeded with aluminium oxide powder particles due to single  
seeder being used and the jet stagnation pressure is measured on the line with  
a Kulite XTE-190M (3.5 bar range) pressure transducer just before the jet  
orifice, prior to experiments with the seeder drum being idle. Pulse separation  
between laser pulses,  $\Delta t$ , is set to 0.6  $\mu$ sec so that sufficient displacement for the  
220 tracer particles of between 4.5 to 10 pixels for the velocity range from 300 m/s

to 750 m/s is achieved. The camera sees a Field of View (FoV) orthogonally

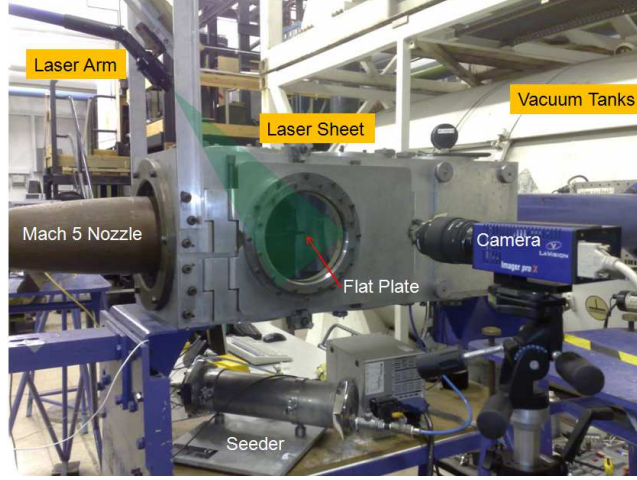


Figure 4: PIV setup.

to the laser sheet. The flowfield is imaged in the streamwise (x) and wall-normal (y) directions over a FoV of approximately  $64 \times 48 \text{ mm}^2$ , resulting in a digital resolution of approximately 25 pixels per mm. A dataset of around 100  
 225 instantaneous vector fields is acquired during the test time at 15 Hz. Each test is repeated 3 times with very good repeatability and a bigger data set including at least 250 instantaneous vector fields is consolidated, excluding under or over-exposed images. Recorded images are divided into initial interrogation areas (IAs) and then processed with a cross correlation algorithm using DaVis 7.2  
 230 software. The initial interrogation areas are selected as  $32 \times 32 \text{ pixel}^2$  with 2 passes and then refined to  $16 \times 16 \text{ pixel}^2$  with 3 passes. 75% overlap is employed in order to improve spatial resolution to yield smoother streamlines. With this arrangement, two adjacent velocity vectors are separated by approximately 0.2 mm. A median filter is applied to correct for spurious vectors. The median  
 235 filter computes a median vector from 8 neighbouring vectors and compares the middle vector with this median vector  $\pm$  deviation of the neighbouring vectors. The centre vector is rejected when it is outside the allowed range of the average vector  $\pm$  deviation of the neighbouring vectors. This rejected vector is iterative

replaced using a 4-pass regional median filter. It is essential that it is applied  
 240 when calculating averages and standard deviations [35]. FoV averaged Signal  
 to Noise Ratio (SNR, the ratio of the first correlation peak to the second peak)  
 is found to be better than 2.6, which is deemed to be very good quality [35].  
 Vector validation scheme discards any vector with a SNR value under 1.8.

### 3. Results

#### 245 3.1. Upstream conditions

Different experimental conditions have been studied corresponding to three  
 different momentum flux ratios,  $J$ . The flow conditions for the tests are tabu-  
 lated in Table 2 together with the associated experimental uncertainties found  
 using an approach from Moffat [36]. These conditions are deduced from  $p_0$ ,  $p_{0jet}$   
 250 and  $T_0$  signals. Stagnation pressure signals for the cross flow and the transverse  
 jet flow for tests 1-3 are shown in Fig. 5 with the ensemble-averaging window  
 for PIV data reduction. Useful flow time is reached 0.6 sec after the flow starts.  
 $p_0$  signal for HSST varies less than 1% from 0.6 sec to 7.8 sec whereas  $p_{0jet}$   
 signals vary less than 0.1% throughout the measurement period.

Table 2: Experimental test conditions.

Test	$p_0$	$T_0$	$Re/m$	$Re_{Djet}$	$J$
No	(mbar)	( $^0K$ )	$\cdot 10^6(1/m)$	$\cdot 10^3$	
1(low)	6460	372	13.11	19.6	1.16
2(mid)	6490	375	13.0	46.5	2.75
3(high)	6430	375	12.96	88.5	5.30
	$\pm 0.7\%$	$\pm 2.0\%$	$\pm 3.5\%$	$\pm 2.8\%$	$\pm 4\%$

#### 255 3.2. Conventional/high speed schlieren photography

Figure 6 shows the long exposure (286  $\mu$ sec) schlieren images of the flowfield  
 for the tests 1-3. A leading edge shock due to viscous interaction and a laminar

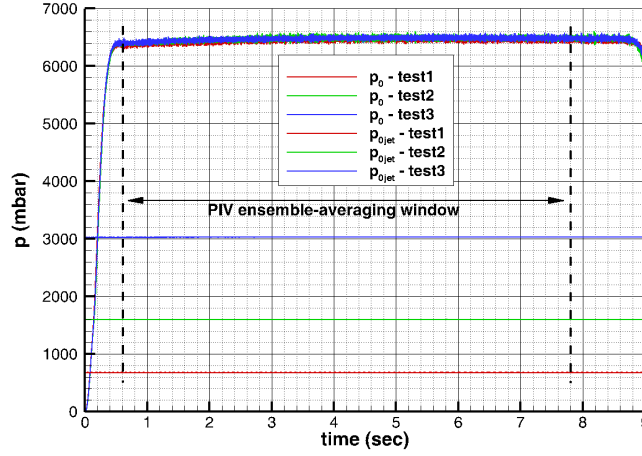


Figure 5: Stagnation pressure histories for tests 1-3.

boundary layer growing up to the separation point and then being diverted in the vertical direction thereafter, can be observed clearly. The high speed boundary layer developing on the flat plate before the jet induced separation within the achievable range of unit Reynolds numbers, is laminar unless tripped [31]. Whereas the jet flow is turbulent for the range of Reynolds numbers (see Table 2). Due to the separation of the incoming laminar boundary layer, transition to turbulence is likely to occur within the upstream separation regions. The cause of this phenomenon is the extreme sensitivity of the separated shear layer to disturbances [37]. Separation shock emanates around the separation point and intersects the jet induced bow shock. The sonic jet expands suddenly and bends downstream, afterwards its expansion is terminated by the Mach disc. The maximum vertical position of the Mach disc is taken as the Mach disc height,  $h$ . The nearfield boundary of the jet is confined within the barrel shocks. The separation region, separation shock and bow shock are three dimensional curved flow structures around the transverse jet. These three dimensional flow structures are superimposed on schlieren images and are well reported in the literature and mentioned in Section 1. The transverse jet penetrates further for higher values of  $J$ , the bow shock moves away from the surface and the separation region extends in both upstream and downstream directions. The

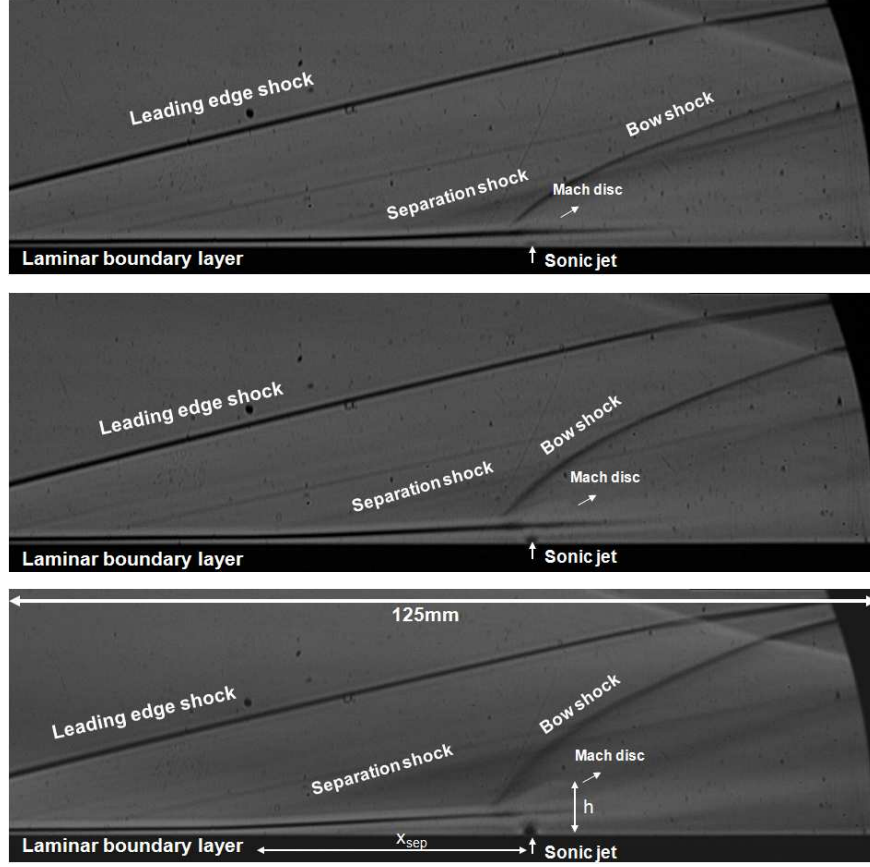


Figure 6: Schlieren visualisation of the flowfield in the presence of the sonic transverse jet with three different momentum flux ratios; top: test 1, middle: test 2, bottom: test 3 with annotated flow structures.

Mach disc height,  $h$ , and the separation length,  $x_{sep}$ , can be extracted from the schlieren images using digital image processing. The Mach disc height is compared to a theoretical estimate from Cassell [38], which is shown in Eqn. 6.

280  $C_d$  is the discharge coefficient of the sonic jet with values around 0.96-0.98 for the range of jet Reynolds numbers considered. These values are tabulated in Table 3. The agreement is found to be good since jet penetration height is governed heavily by  $J$ . In addition, the stagnation conditions for both the jet and the free stream are quite steady (less than 1% variation) during the useful running

time of the HSST and they are known accurately. In terms of the extent of the separation region, it is taken as the distance between where boundary layer starts to deviate from the main flow direction (due to separation shock) over  $0.5 \pm 0.2$  degrees with respect to horizontal and the centre of the jet orifice. The separation shock angle is measured to be 13 degrees with respect to flat plate surface, whilst the boundary layer has deviated nearly 3 degrees with respect to flat plate surface. At Mach 5, 3 degrees flow deflection causes an oblique shock wave to occur at 13.6 degrees theoretically, hence the experimental value is consistent with theory.

$$\frac{h_{theo}}{d_{jet}} = \frac{1}{M_\infty} \sqrt{\frac{2p_{0jet}\gamma_{jet}}{C_d p_\infty \gamma_\infty}} G \quad (6)$$

where

$$G = \left[ \frac{2}{\gamma_{jet} - 1} \frac{2}{\gamma_{jet} + 1}^{(\gamma_{jet} + 1/\gamma_{jet} - 1)} H \right]^{1/4}$$

and

$$H = \left\{ 1 - \frac{p_\infty}{p_{0jet}}^{(\gamma_{jet} - 1/\gamma_{jet})} \right\}$$

Table 3: Experimental and theoretical Mach disc heights ( $h$ ) and experimental separation lengths ( $x_{sep}$ ) tests 1-3.

Test	$h$	$h_{theo}$	$x_{sep}$
No	(mm)	(mm)	(mm)
1 (low)	$4.3 \pm 0.2$	4.1	$22.8 \pm 0.3$
2 (mid)	$6.2 \pm 0.2$	6.3	$38.2 \pm 0.3$
3 (high)	$8.0 \pm 0.2$	8.4	$41.8 \pm 0.3$

The Mach disc height non-dimensionalised by the jet diameter,  $h/d_{jet}$ , against  $J$  and the separation distance non-dimensionalised by the jet diameter,  $x_{sep}/d_{jet}$ , against the Mach disc height non-dimensionalised by the jet diameter,  $h/d_{jet}$ , are plotted in Fig. 7. A power law fit is applied for Mach disc height and the resultant equation is specified in the figure. The penetration increases with increasing momentum flux ratio however the trend is non-linear. This finding

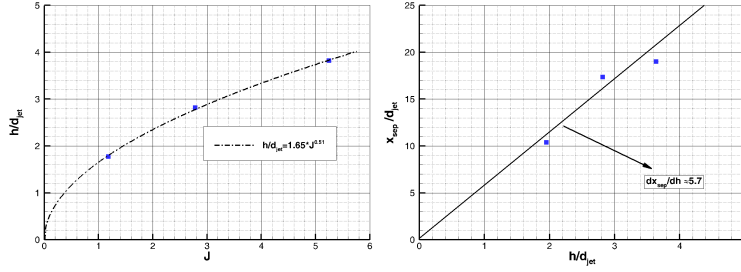


Figure 7: Left: Mach disc height non-dimensionalised by jet diameter versus momentum flux ratio; right: separation distance non-dimensionalised by jet diameter versus Mach disc height non-dimensionalised by jet diameter for tests 1-3.

is consistent with the results by Papamoschou and Roshko [39]. Their results showed that the penetration behaviour of a sonic/supersonic jet through a circular hole into high speed crossflow is not dramatically different to that of a subsonic jet penetration into subsonic cross flow, where square root relationship can be observed for jet penetration height. Both Mach disc height and separation length exhibits similar behaviour with momentum flux ratio, therefore if these are plotted against each other the effect of momentum flux ratio is taken out. Only the dependence on the state of the boundary layer appears and a nearly linear behaviour is obtained with a slope of around 5.7. The extent of the separation region is strongly governed by the state of the incoming boundary layer as the bow shock induces adverse pressure gradient and causes it to separate. In this case the boundary layer is laminar thus it is less resistant to an adverse pressure gradient and separates earlier than it would for a turbulent boundary layer [31].

As mentioned in Section 1, the interaction of the transverse jet with the incoming flow is unsteady owing to jet shear layer instabilities. In the region near the injector exit, the injectant fluid moves with a higher vertical velocity tangentially to the interface than the incoming flow. As a result, large vortices are periodically formed engulfing large quantities of free stream fluid and drawing it into the jet shear layer and then are convected downstream. These large scale coherent structures are dominant in the jet shear layer and their structural

evolution might have a big influence on the jet near field [10]. It is therefore  
 important to understand how these structures and their growth rates change  
 325 in time. High speed schlieren photography reveals these structures captured at  
 16 kfps with 1  $\mu$ sec exposure as they are shown in Fig. 8 for test 3. Several  
 interesting features, such as the large scale structures at the jet periphery and  
 the distorted bow shock are apparent in the images. The bow shock stand-  
 off distance is very small, it is almost merged within the expanding jet, and  
 330 curves sharply downstream. The local shape of the bow shock appears to de-  
 pend strongly on the convection of large scale shear layer structures, especially  
 close to the jet exit where local flow behind the bow shock is subsonic. Fur-  
 thermore the separation shock is also unsteady due to the disturbances, in the  
 vicinity of the jet injection that are fed upstream through the subsonic portion  
 335 of the boundary layer. The barrel shock and the Mach disc are, however, not  
 very clear in the short exposure schlieren images, due to the unsteadiness. The  
 eddies forming in the shear layer are part of the unsteady Kelvin-Helmholtz  
 spanwise rollers wrapping around the jet. They are the traces of three dimen-  
 sional transverse vortex tubes whose cores coiled up around the jet with their  
 340 legs connected downstream of the jet exit [10].

Root Mean Square (RMS) of the fluctuations in the light intensity based on  
 1000 schlieren images, which show different levels of penetration and signify the  
 high levels of unsteadiness, are shown in Fig. 9 for each  $J$  value. The jet upper  
 boundary can be easily seen and high amplitudes of RMS are observed to occur  
 345 in the flow domain occupied by the fluctuating bow shock and the windward  
 side (upstream side) of the barrel shocks. It has to be noted that the evolution  
 of coherent jet shear layer vortical structures can not be discussed here because  
 of the long interframe time of the schlieren recording, which is 62.5  $\mu$ sec. The  
 leading edge shock is observed as a very thin line (the unsteadiness is minimal),  
 350 which demonstrates the good flow quality at upstream conditions.



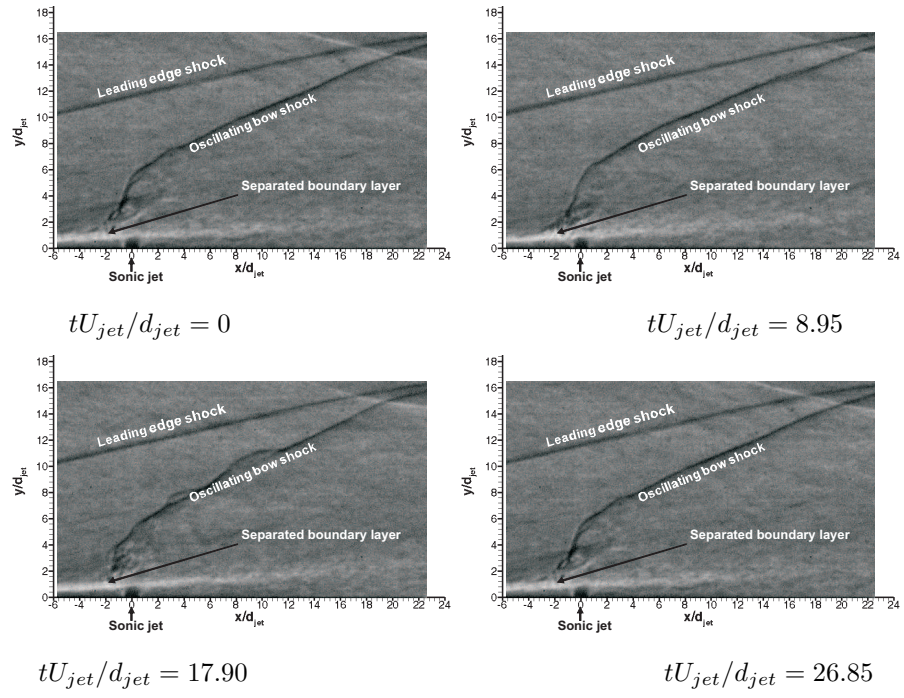


Figure 8: High speed schlieren visualisation of the sonic transverse jet captured at 16000fps with 1  $\mu sec$  exposure time and annotated flow structures for test 3.

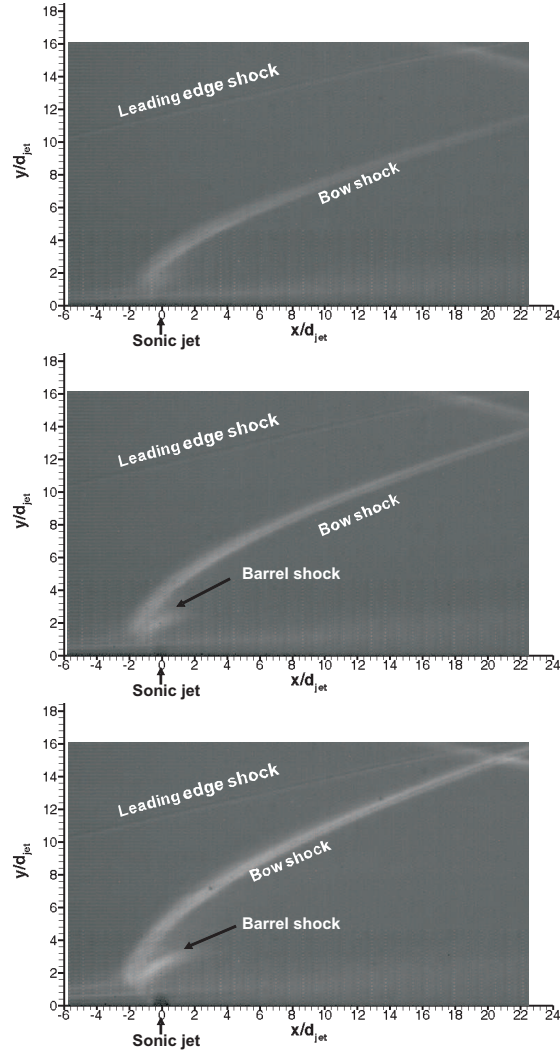


Figure 9: RMS of instantaneous schlieren images of a time series of 1000 samples with annotated flow structures; top: test 1, middle: test 2, bottom: test 3.

### 3.3. Wall Pressure Measurements

Figure 10 shows non-dimensional wall pressure distributions against non dimensional distance, i.e  $(x - x_{jet})/d_{jet}$ , for different momentum flux ratios at centreline,  $z/d_{jet}=4.77$  and  $z/d_{jet}=9.1$  for tests 1-3. The theoretical estimate  
 355 using viscous interaction for slightly cold wall is also shown in Figure. The

details of the viscous interaction can be found in Reference [26]. In addition the data without the jet is also plotted.

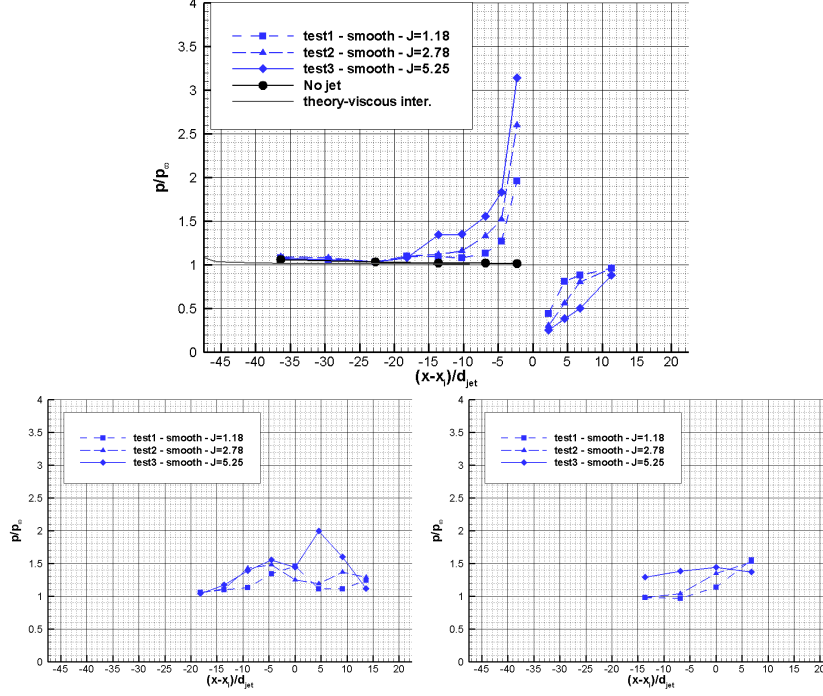


Figure 10: Non dimensional wall pressure distribution against non dimensional distance at the centreline (top),  $z/d_{jet}=4.77$  (bottom left) and  $z/d_{jet}=9.1$  (bottom right) for test 1-3.

In theory the wall pressure along at the leading edge is slightly higher than the free stream pressure reaching 1.1 times  $p_\infty$  due to viscous interaction and gradually decreases to free stream value. This behaviour is also observed in experiments with slight overshoot, which might be due to experimental uncertainty. The non-dimensional pressure values are found to be accurate within 5%. After the gradual decrease, the wall pressure starts to increase from the point at which the flow separates, and then there is further rise to a pressure plateau. The pressure rise due to the injection does not become apparent until a  $(x - x_{jet})/d_{jet}$  value of -20 for test 3, afterwards it rises gradually implying laminar separation. The rise is rather abrupt for turbulent boundary layers, thus proof of the existence of laminar boundary layer. Generally, for a laminar

boundary layer, the separation region due to adverse pressure gradient is larger  
 370 than the one for a turbulent boundary layer due to its less resistive nature; hence  
 it separates earlier than a turbulent boundary layer. This rise is followed by the  
 peak at the upstream of the jet reaching nearly 3.2 for highest  $J$  value. Down-  
 stream of the jet the pressure well is apparent that is accompanied by a rise due  
 to recompression shock. The non dimensional pressure in the downstream of the  
 375 jet does not exceed 1 for hypersonic interactions. Each plot exhibits the effect  
 of increasing jet to free stream momentum flux ratio which leads to increase in  
 the wall static pressure values at both upstream and downstream regions. The  
 size of upstream and downstream flow structures extent not only in streamwise  
 direction but also in the spanwise direction, spreading laterally with higher  $J$   
 380 values. The magnitude of the peak pressure on the  $z/d_{jet}=4.77$  off-centreline is  
 found to be around 2 at  $x/d_{jet}=5$ .

### 3.4. PIV

#### 3.4.1. Assessment of PIV technique

To assess the particle response time experimentally, an oblique shock wave  
 385 test [17]-[19] or a blunt body normal shock wave test [40] are frequently used.  
 However the lack of a standing oblique shock for this flowfield suggests the  
 use of a Mach disc (a normal shock) instead. Even though the acceleration  
 of the flow before and after the Mach disc introduces uncertainty in terms of  
 the velocities before and after shock, the possibility of the ensemble averaging  
 390 during the useful running time of HSST diminishes the amount of uncertainty  
 in ensemble-averaged flow field. This is due to the fact that the uncertainty in  
 mean velocity is inversely proportional to the square root of the ensemble size.  
 Ragni et al. [42] described two critical parameters, as spatial ratio,  $SR$ , and  
 temporal ratio,  $TR$ , for the experimental measurement of the particle response  
 395 time. The expressions for these parameters are specified in Eqn. 7.  $IA$  is the  
 size of the final interrogation area and  $\xi_p$  is the relaxation distance.

$$SR = \frac{IA}{\xi_p} \quad \text{and} \quad TR = \frac{\Delta t}{\tau_p} \quad (7)$$

For a PIV experiment, the conditions for  $SR, TR \leq 1$  can be considered acceptable for an accurate measurement of the tracer response time [42]. This condition has implications on the required seeding concentration and digital  
400 imaging resolution as well as on the time separation between exposures. In the previous work of the authors [16],  $SR$  and  $TR$  values were found after measuring  $\xi_p$  and  $\tau_p$  values from the ensemble-averaged flow field and the conditions for  $SR, TR$  were satisfied.

### 3.4.2. Start-up behaviour and instantaneous flow structures

Figure 11 shows the raw PIV images captured throughout the test run for  
405 test 2 as mentioned in Ref. [16], yet for the sake of completeness they are shown in here. In the experimental test campaign the transverse jet is started just before the test gas arrival. In that time the jet discharges nearly vertically (minimum effect of the vacuum downstream) due to significant initial jet momentum  
410 flux ratio. Afterwards with the arrival of the freestream test gas, transverse jet bends towards the main direction of the freestream flow, in the horizontal direction,  $x$ . Unsteadiness of the jet trajectory and jet shear layer instabilities are observed clearly. Periodically formed large vortices engulf large quantities of incoming air, drawing it into the jet shear layer, and then are swept down-  
415 stream. It is evidently clear that due to their inertia, particles get dispersed around the bow shock making bow shock and jet shear layer visible. After the useful running time has passed (around 7.2sec), severe oscillations start to occur in the jet flow as Mach 5 flow no longer exists and finally when the firing valve is closed (when there is no cross flow) the jet discharges nearly vertically. The  
420 early termination of useful running time (7.2 sec instead of 7.5 sec) is attributed to the fact that a constant mass flow rate of the secondary jet is increasing the mass flow rate going inside the vacuum tanks, and hence increasing the back pressure. Figure 12 shows selected raw PIV images (first frames only) and the corresponding velocity vector fields for tests 1-3 with increasing  $J$  value. The  
425 velocity vectors are coloured by non-dimensionalised velocity magnitude, i.e.  $\sqrt{u^2 + v^2}/U_{jet}$ . The jet orifice is located at the origin and the horizontal and

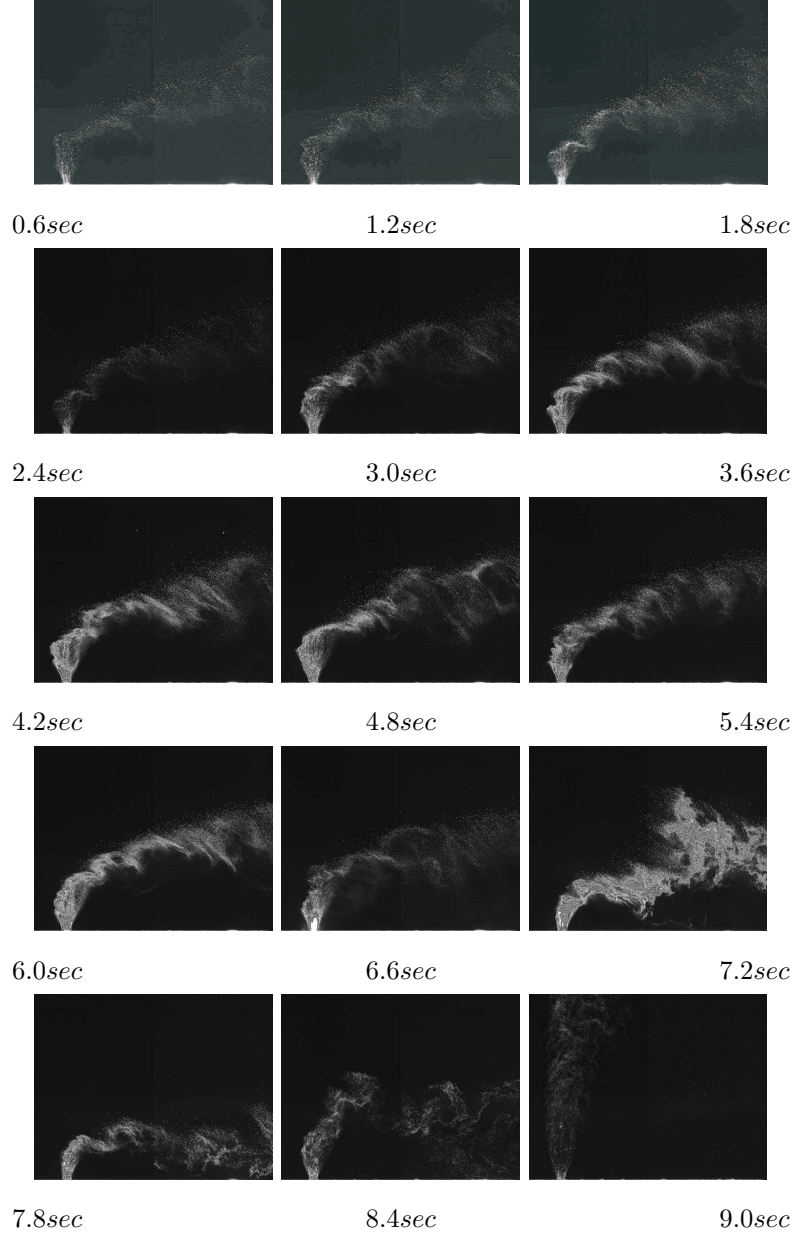


Figure 11: PIV raw image visualisation of the sonic transverse jet captured at 15 Hz for test 2 during the running time of HSST. Only the first frames of the PIV recordings are shown.

vertical coordinates are normalized with the jet diameter,  $d_{jet}$ . The time that elapses between consecutive recordings (66 msec) is significantly larger than the jet flow characteristic time scale of around 70  $\mu$ sec, leading to the measurement of uncorrelated velocity fields. As the jet is discharged from the orifice, at a velocity around 315 m/s, acceleration of the flow in the transverse direction is observed and this acceleration is terminated by the Mach disc, which bends the jet flow in the freestream flow direction. After the Mach disc, the jet velocity is reduced and this reduction is followed by an acceleration with velocities reaching 750 m/s, which is close to the free stream velocity but slightly lower due to the presence of the bow shock. With increasing momentum flux ratio, the transverse jet spreads wider, exhibiting higher levels of penetration and forming a thicker jet affected area as expected. The presence of bow shock is also apparent, where the deceleration through it, is smeared due to finite IA size, a natural artefact of PIV correlation. In addition, an interesting observation is that the upper jet boundary is extending over the bow shock, which means the particles are spreading over the bow shock. The reason for that might be due to the inertia of the solid particles as they are discharged vertically from the jet orifice and some of them can not adjust themselves as smoothly as air jet flow.

### 3.4.3. Raw PIV image analysis

Root Mean Square (RMS) of raw PIV images based on 250 samples, which show different levels of penetration and jet trajectories, are shown in Fig. 13 for each  $J$  value. The first frames of PIV recordings are used for this analysis. The advantage of this technique against processed PIV analysis is that the jet boundaries can be located more accurately, independent of the size of IA that is used for processed PIV analysis. The simplified jet boundaries are drawn using edge detection filtering and are shown with dashed lines. For tests 1 and 3 some of the particles are convected in upstream direction, which is believed to be due to the upstream propagation of jet flow into the separation region through the boundary layer. Higher amplitudes of RMS are observed to occur in the jet near field. The barrel shocks are clearly observed on the windward and the leeward

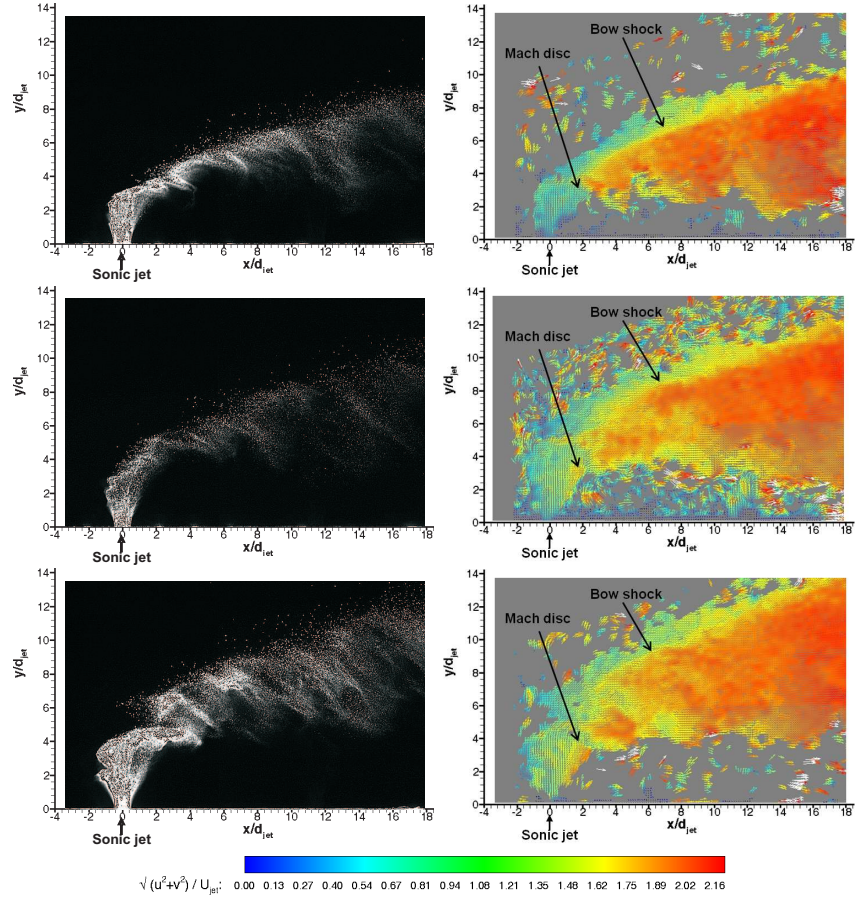


Figure 12: Instantaneous raw PIV images (left) and associated vector fields (right); top: test1, middle: test2, bottom: test 3. Only the first frames of the PIV recordings are shown on the left.



sides of the jet flow. As the momentum flux ratio is increased the jet boundary and the bow shock extend in transverse direction as expected.

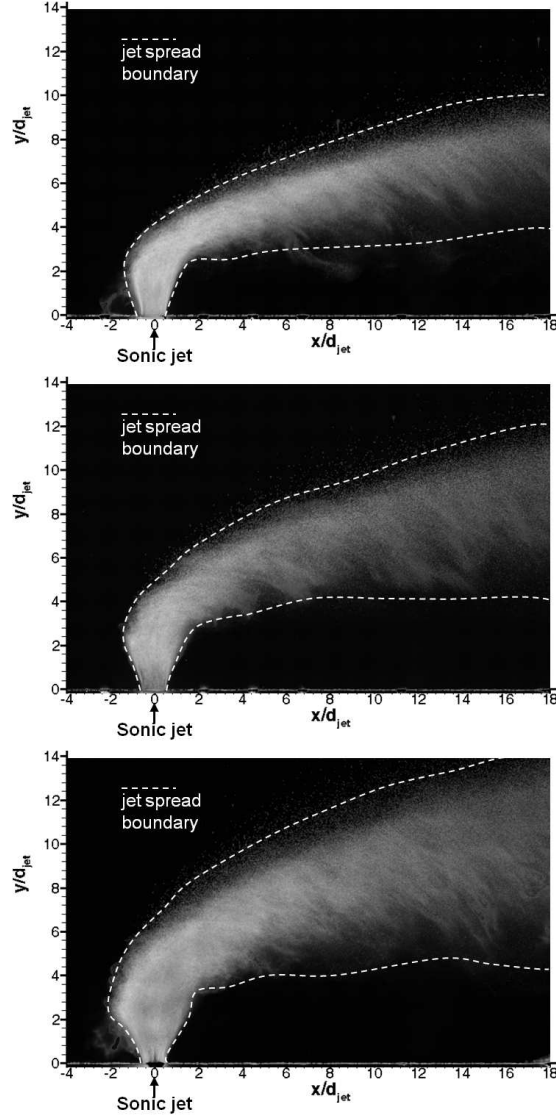


Figure 13: RMS of instantaneous PIV images of a time series of 100 samples with jet boundaries; top: test 1, middle: test 2, bottom: test 3.

Figure 14 shows the RMS of instantaneous PIV images overlaid on to RMS  
of instantaneous schlieren images (see Fig. 9). This is done to compare different

measurement techniques. The agreement is found to be very good, the near field jet structure is coincident with different measurement techniques. An interesting observation is that the upper jet boundary is extending over the bow shock, which means the particles are spreading over the bow shock. The reason for that might be two-fold: inertia of the solid particles as they are discharged  
465 vertically from the jet orifice and some of them can not adjust themselves as smoothly as air flow, or the mutual interaction of the jet shear layer vortices (due to Kelvin-Helmholtz instabilities) with the bow shock. The latter is quite likely as these vortices are responsible for distorting the local shape of the bow  
470 shock as explained in Section 3.2. Therefore the mixing of jet flow with the crossing flow can occur over the bow shock as the free stream entrains inside the jet stream and vice-versa, which is also reported by Ref. [10].

#### 3.4.4. Mean flow organisation

Figures 15 to 16 show non-dimensionalised streamwise and transverse velocity contours, i.e.  $\langle u \rangle / U_{jet}$  and  $\langle v \rangle / U_{jet}$ , for tests 1-3 ensemble-averaged  
475 over 250 instantaneous vector fields. The brackets,  $\langle \rangle$ , refer to ensemble-averaged quantities. The streamlines are also visualised. Leaving the jet orifice, the transverse jet expands depending on the back pressure behind the jet induced bow shock. On the windward side (upstream side), the jet turns quickly  
480 towards the main flow direction, whereas on the leeward side (downstream side) turning behaviour is more gradual. On the leeward side the termination of the jet expansion (Mach disc) is especially apparent for tests 2 and 3. Negative streamwise velocities are observed on the windward side of the jet stream in Fig. 15, whereas negative transverse velocities are observed in the farfield on  
485 the bottom region (Fig. 16). Penetration is clearly increased with increasing momentum flux ratio and the transverse spread is enhanced. Due to the low levels of seeding outside the jet boundaries the data is likely to include some level of bias towards the velocity values in the regions with sufficient seeding density. This velocity bias is most likely to tend to approach to the transverse  
490 velocity component in the jet nearfield whereas in the farfield it is expected to

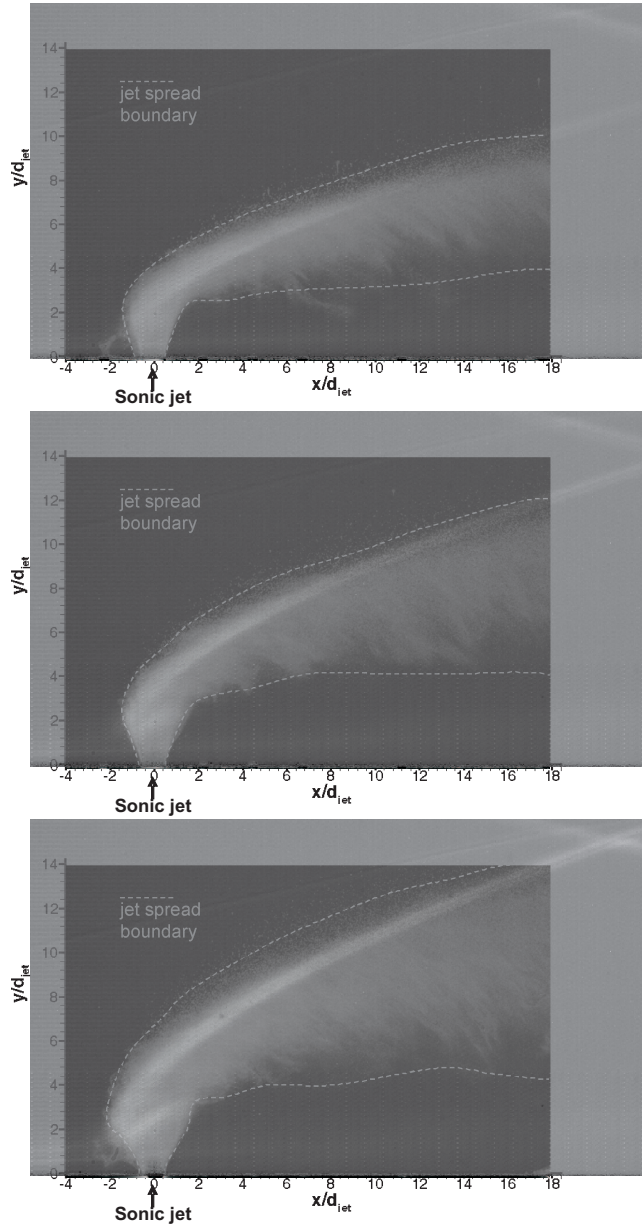


Figure 14: RMS of instantaneous PIV images of a time series of 100 samples overlaid on to RMS of instantaneous schlieren images of a time series of 1000 samples; top: test 1, middle: test 2, bottom: test 3.

tend to approach towards the streamwise velocity component. Therefore the data outside the jet boundaries or outside the streamlines is questionable in absolute terms. In order to identify prominent flow structures in detail, mean velocity magnitude contour lines are plotted in Fig. 17 for test 3 and compared  
495 with the numerical simulations from Viti et. al [43]. From PIV measurements, the windward and leeward sides of the barrel shock are clearly present. The presence of the bow shock is visible as the contour lines stay parallel around it. On the other hand the reflected shock is linked to the Mach disc on the leeward side of the barrel shock. This is similar to the findings of Viti et. al [43] even  
500 though  $J$  is 17.5 for that study.

Figure 18 shows the mean velocity magnitude profiles at  $x/d_{jet} = 2, 5, 10, 15$  and 20 for tests 1-3. The locus of maximum velocity is a curved line and its height from the wall is initially decreasing with the streamwise distance in the nearfield and afterwards it starts to increase in the farfield. This phenomenon is  
505 observed for tests 2 and 3, whereas for test 1, a continuous monotonic increase is observed. After the Mach disc, the jet loses most of its momentum and gets carried away with the cross flow. In the nearfield, i.e.  $x/d_{jet} = 2$ , velocity profiles show a sharp peak and in the farfield the peak broadens and spreads in the vertical direction. There are fluctuations observed around  $2|y/d_{jet}|4$ ; these  
510 are coming from the fact that jet boundaries for all tests are located very near to the region. Hence there is a lot shear in the vicinity as it can be seen from Figure 19. In order to smoothly capture these areas cross flow needs to be seeded with particles.

#### 3.4.5. Turbulence properties

Figure 19 shows the sum of RMS of streamwise and transverse fluctuations  
515  $(\sqrt{\langle u'^2 + v'^2 \rangle}/U_{jet})$ , i.e. turbulence intensity (TI)) contours over 250 instantaneous vector fields for tests 1-3 during the useful running time of HSST. These results reflect the mixing that takes place within the interaction of the jet with the freestream flow and the distributed nature of the turbulence. As  $J$  is in-  
520 creased the extent of the local jet boundary (drawn in black dotted lines, which

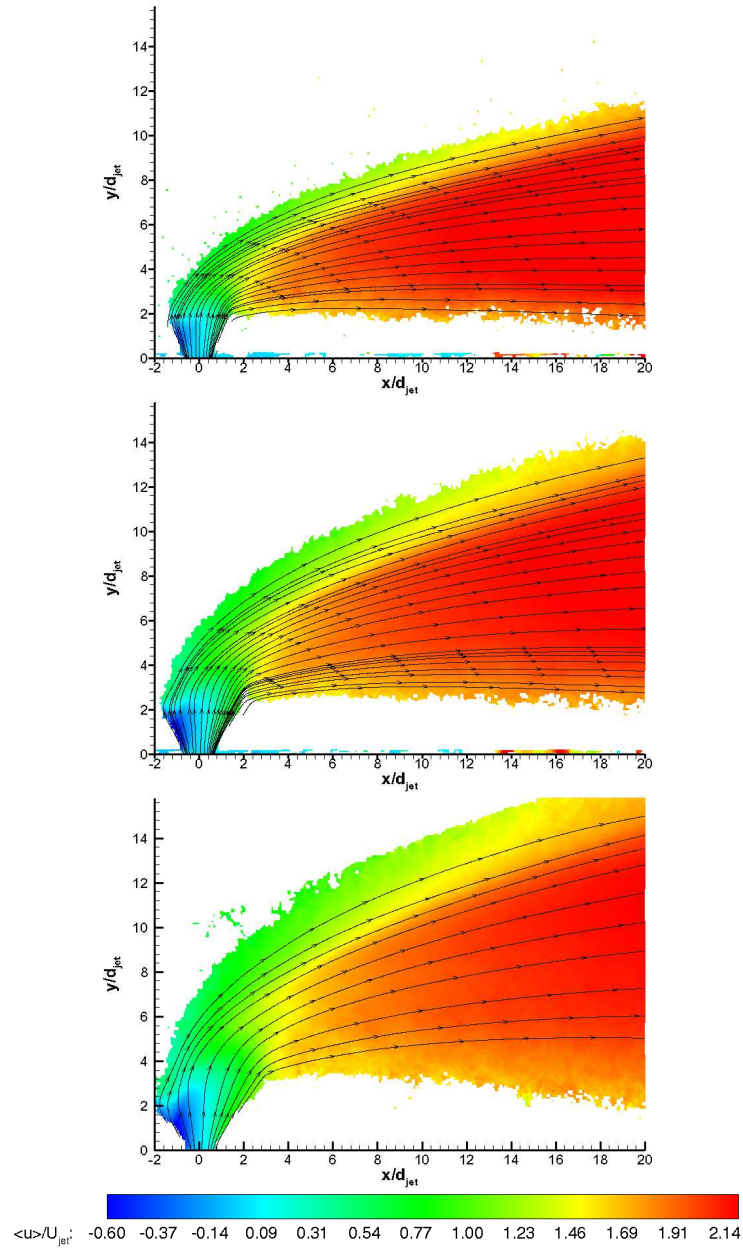


Figure 15: Mean streamwise velocity  $\langle u \rangle / U_{jet}$  contours with streamlines; top: test1, middle: test2, bottom: test 3.

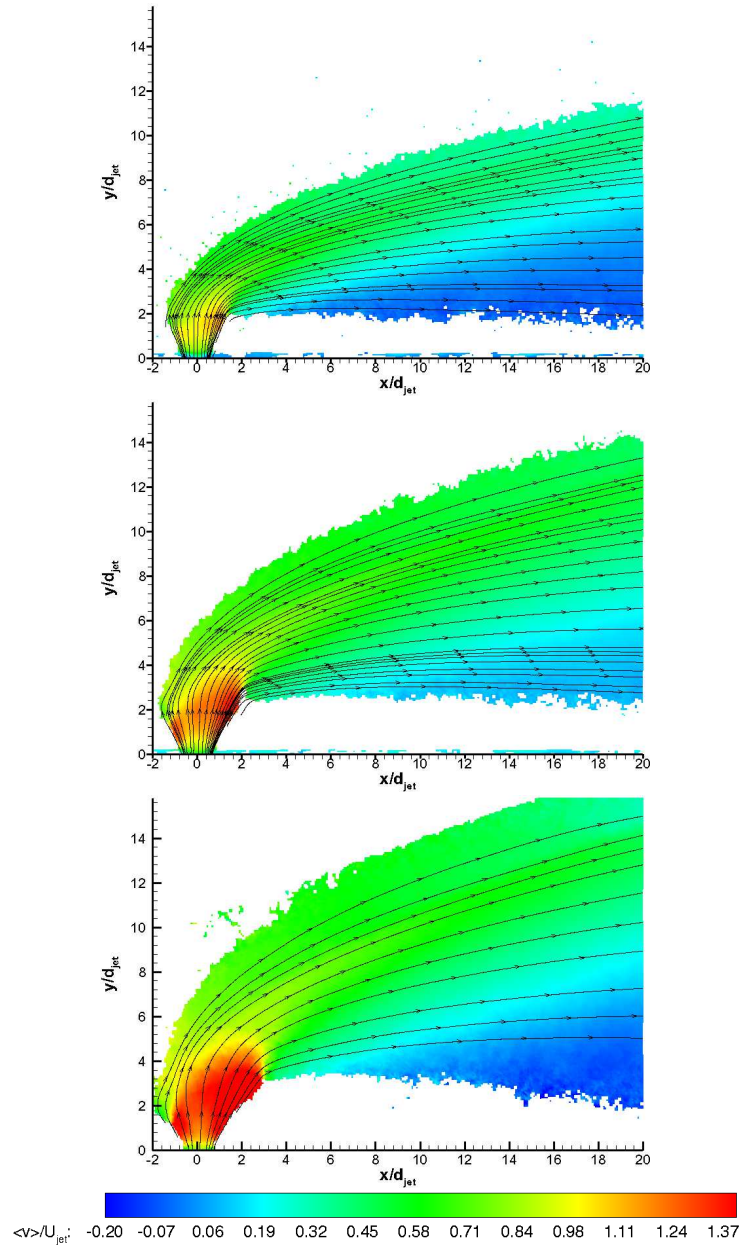


Figure 16: Mean transverse velocity  $\langle v \rangle / U_{jet}$  contours with streamlines; top: test1, middle: test2, bottom: test 3.

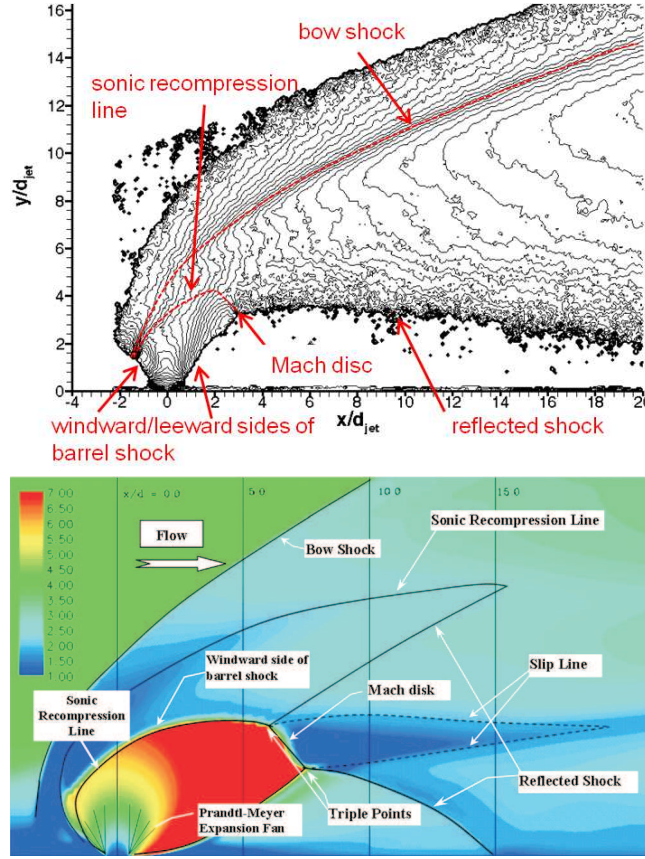


Figure 17: Top: mean velocity magnitude contour lines for test 3, bottom: the detailed flow field around the jet orifice with the main flow features highlighted with solid lines from Viti et. al [43].

is composed of the barrel shocks and Mach disc) is increasing in size, and the extent of jet spreading (drawn in black dashed lines) is growing. The barrel shocks and the Mach disc forming the jet boundary are visualised/quantified for the first time in open literature using PIV measurement technique. The upper boundary of the jet spreading is defined by the maximum penetration of shear layer vortices interacting with the bow shock. On the other hand the lower boundary of the jet spreading is defined by the mixing of the jet stream above the wake vortices mentioned Section 1. These boundaries are already defined in Section 3.4.3 using raw PIV image analysis and transferred to TI contours.



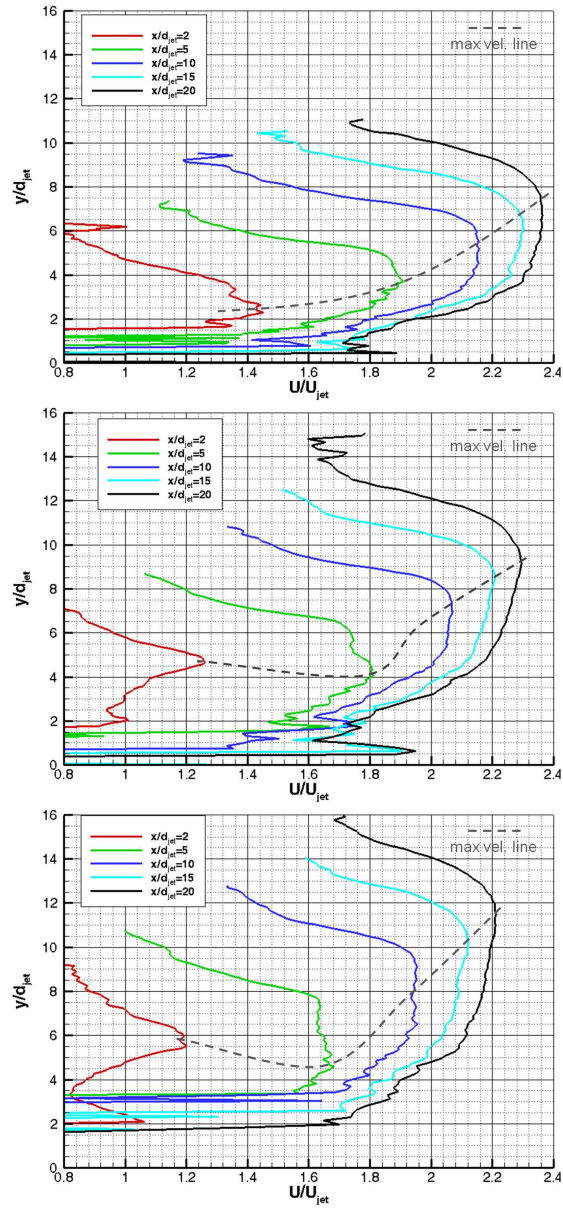


Figure 18: Mean velocity magnitude profiles at various locations; top: test1, middle: test2, bottom: test 3.

530 Substantial increase in TI occurs outside jet spreading boundaries, especially above the bow shock and below the reflected shock, leading to non-physical



turbulence information (an artefact of PIV image correlation in the absence of necessary particle population). Therefore a TI threshold value is applied to discard these regions, which is taken as 15 %. As mentioned in Section 3.4.4 the data outside the jet boundaries is questionable in absolute values owing to low seeding density. The penetration bandwidth can be related to the difference between the extents of the jet spreading boundary. For tests 1-3 the Mach disc height and the penetration height at  $x = 20d_{jet}$  are tabulated in Table 4. The Mach disc height values are in very good agreement with the values found from the schlieren images as well as the theoretical estimates from Eqn. 6. However the uncertainty in  $h$  is found to be  $\pm 0.5$  mm. This uncertainty is mainly due to the finite response time of the particle in transverse air jet flow and the finite IA size. Inside the barrel shocks and Mach disc lower values

Table 4: Experimental and theoretical Mach disc heights ( $h$ ).

Test No	$h_{sch}$ (mm)	$h_{PIV}$ (mm)	$h_{theo}$ (mm)	$H$ at $x = 20d_{jet}$ (mm)
1 (low)	$4.3 \pm 0.2$	$4.6 \pm 0.5$	4.1	$18.0 \pm 0.5$
2 (mid)	$6.2 \pm 0.2$	$6.4 \pm 0.5$	6.3	$21.1 \pm 0.5$
3 (high)	$8.0 \pm 0.2$	$8.8 \pm 0.5$	8.4	$26.0 \pm 0.5$

of TI are observed. Significant amount of turbulence occurs above the Mach disc, which might be due to the shear layer shown numerically by Viti et. al [43]. However in the centre of the jet penetration band turbulence decays starting from approximately at  $x/d_{jet}=4$  for tests 1 and 2 and  $x/d_{jet}=5$  for test 3 extending to the farfield. Furthermore high turbulence is also occurred around the intersection of the windward side of the barrel shock and bow shock.

#### 3.4.6. Quadrant decomposition

The quadrant decomposition of instantaneous velocity fluctuations is examined to obtain more insight into turbulence structures. This decomposition method is commonly used to identify the orientation and qualitative organisa-

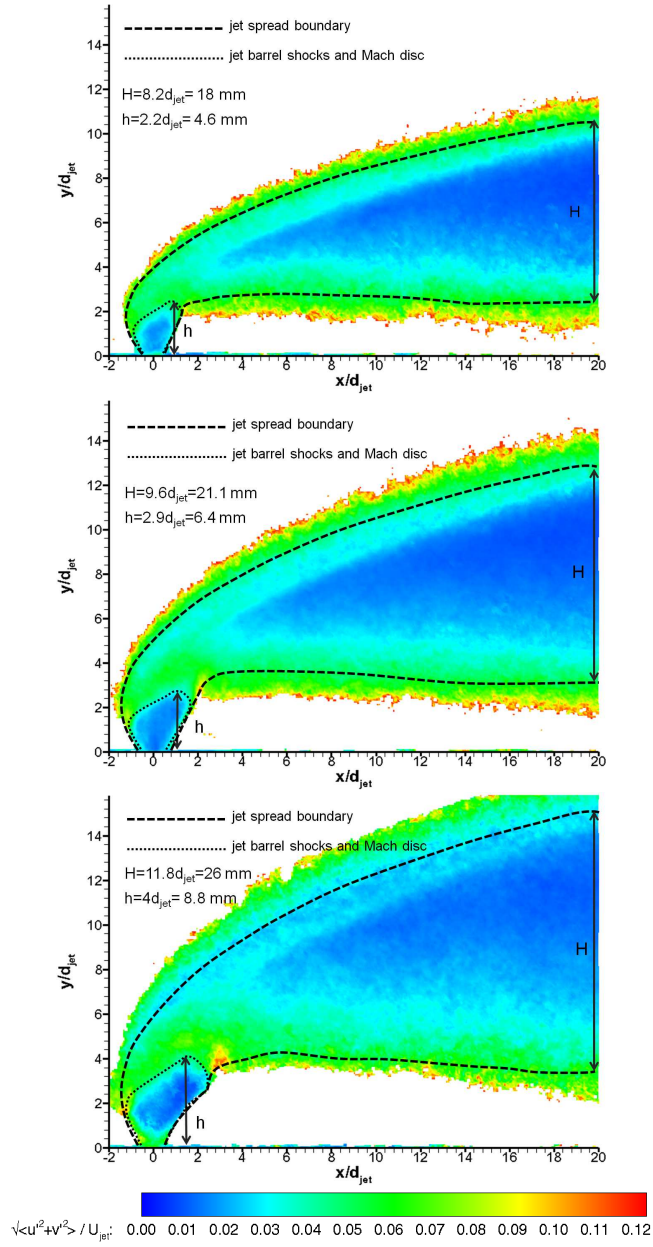


Figure 19: Averaged flow field turbulence intensity contours; top: test 1, middle: test 2, bottom: test 3.

tion of large scale structures. It is done at three probe areas of 1.5 mm<sup>2</sup> size  
 555 (including at least 7 velocity vectors around) in the flowfield; the first probe  
 area is located above the Mach disc, the second one at the jet shear layer below  
 the bow shock and the last one at the jet core downstream in the farfield. The  
 locations of the centres of these areas with respect to the origin, normalised by  
 the jet diameter, are tabulated in Table 5. The instantaneous shear angle,  $\phi$  is  
 defined in Eqn. 8.

Table 5: The locations of the centres of the probe areas normalised by the jet diameter,  $x/d_{jet}$   
 and  $y/d_{jet}$ , for tests 1-3.

Test No	Probe area 1	Probe area 2	Probe area 3
1	(1.3, 2.6)	(5.3, 5.2)	(17.2, 6.2)
2	(2.0, 2.9)	(5.5, 6.4)	(17.3, 8.0)
3	(2.4, 3.8)	(5.3, 8.0)	(17.2, 10.8)

560

$$\phi = \arctan\left(\frac{v'}{u'}\right) \quad (8)$$

The velocity fluctuations are non-dimensionalised by RMS of each component  
 for all probe areas and they are plotted in Fig. 20 for all tests. The histograms  
 of instantaneous shear angle,  $\phi$ , are also plotted based on 250 samples. The  
 first probe area (located above the Mach disc) shows preferred direction in the  
 565 distribution of turbulence for all tests in quadrants 2 and 4. Quadrant 2 stands  
 for decelerating flow ( $u' < 0$ ) with an upward motion ( $v' > 0$ ), whereas quadrant  
 four stands for the opposite. Negative shear angles are found and the preferred  
 direction is found to be around -45 degrees for test 1, -33 degrees for test 2 and  
 -20 degrees for test 3. This phenomenon implies that immediately above the  
 570 Mach disc streamwise fluctuations are more prominent than transverse fluctu-  
 ations in opposite sign. The reason for that might be the sudden deceleration  
 through the Mach disc causing the velocity fluctuations to be damped in ver-  
 tical direction. Nonetheless for test 1 the correlation is found to be weak with  
 peaks at -90 and 90 degrees, compared to tests 2 and 3. The second probe area  
 575 (located at the jet shear layer below the bow shock) exhibits no preferred direc-

tion, therefore manifests the isotropic nature of turbulence. Finally the third probe area (located at the jet core downstream) renders preferred direction that is between to -70 and -80 degrees showing nearly the dominance of transverse fluctuations.

### 580 3.4.7. Uncertainty estimates

The statistical errors in ensemble-averaged mean velocity and turbulence intensity are depicted in Equations 9 and 10. Another source of error is found in the determination of pixel displacement by cross correlation algorithm,  $E_{cc}$ . It is commonly assumed as one tenth of a pixel [41] and is converted to velocity  
585 as 6.7 m/s using digital resolution of 25 pixels per mm and  $\Delta t$  of 0.6  $\mu$ sec. All uncertainty values are normalised by jet velocity,  $U_{jet}$ , and tabulated in Table 6.

$$E_{<U>} = \sqrt{\langle u'^2 + v'^2 \rangle} / \sqrt{m} \quad (9)$$

$$E_{\sqrt{\langle U'^2 \rangle}} = \sqrt{\langle u'^2 + v'^2 \rangle} / \sqrt{2m} \quad (10)$$

where  $m$  is the number of uncorrelated individual vector fields, which is 250.

Table 6: Uncertainty estimates.

Test No	$E_{<U>}/U_{jet}$	$E_{\sqrt{\langle U'^2 \rangle}}/U_{jet}$	$E_{cc}/U_{jet}$
1 (low)	1.6%	1.3%	0.2%
2 (mid)	1.4%	1.1%	0.2%
3 (high)	1.4%	1.0%	0.2%

## 590 4. Acknowledgements

The authors would like to thank Mr. Adrian Walker of Engineering and Physical Sciences Research Council (EPSRC) in the UK for the use of Photron-SA1 monochrome high speed video camera. This work was supported by Defence Science and Technology Laboratory, UK under contract number DSTLX  
595 1000043546.

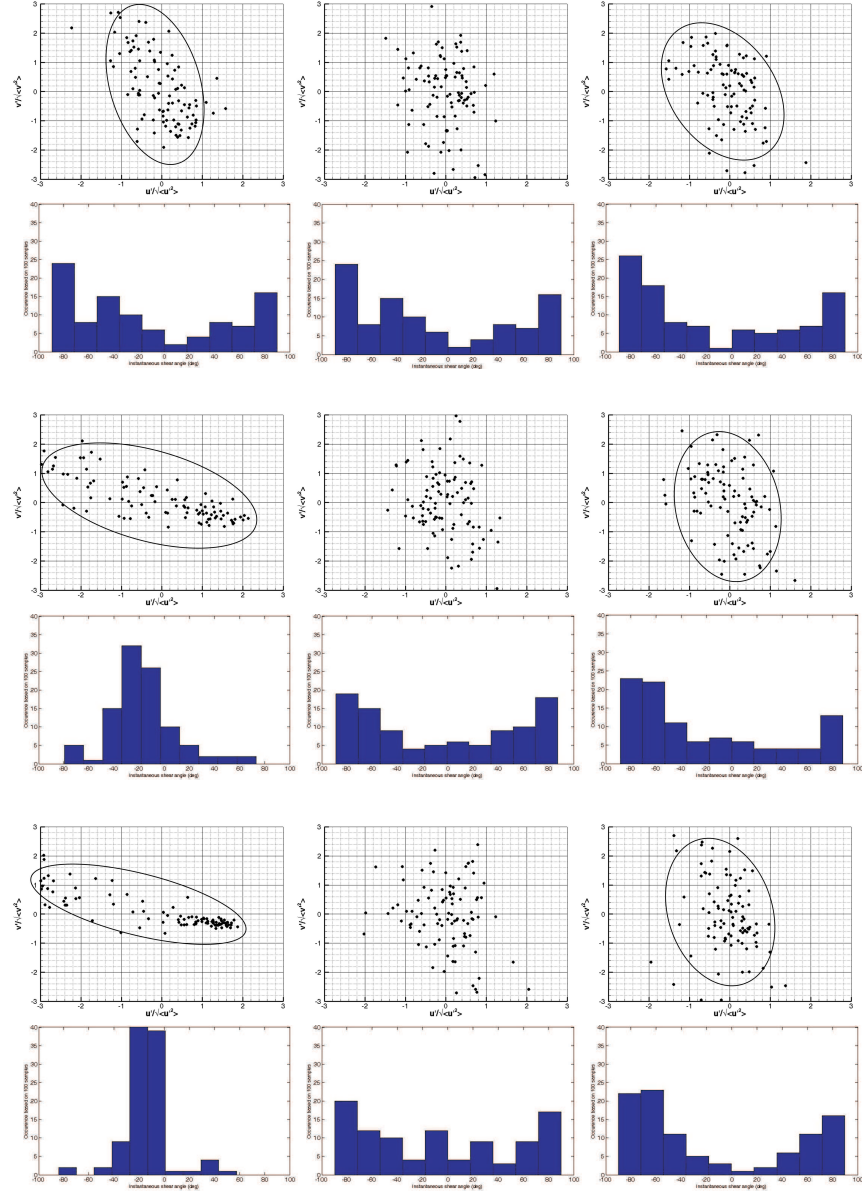


Figure 20: Quadrant decomposition of instantaneous velocity fluctuations for the probe areas 1, 2 and 3 from left to right with corresponding histograms underneath; top: test 1, middle: test 2, bottom: test 3.

## 5. Conclusions

Experiments involving a sonic round jet injected into a high speed cross flow at Mach 5 over a flat plate were carried out. The boundary layer developing on the flat plate was laminar and jet to free stream momentum flux ratio,  $J$ , was varied from 1.16 to 5.30 with a unit Reynolds number set at  $13 \cdot 10^6 \text{1/m}$ . The separation shock and the separation region, the jet induced bow shock and the nearfield boundary of the jet flow composed of the Mach disc and the barrel shocks were observed. As the momentum flux ratio is increased, prominent curved flow structures extent in the upstream and downstream directions. Jet penetration was found to be a non-linear function of  $J$  and the separation location extended upstream 5.7 times the penetration height. High speed schlieren visualisation revealed the oscillating structure of the bow shock. The local shape of the bow shock appeared to depend strongly on the convection of large scale shear layer structures, especially close to the jet exit where the local flow behind the bow shock was subsonic. Steady wall pressure measurements revealed the interaction region between the jet and the incoming cross flow developing on the flat plate, in line with schlieren visualisation.

To assess the jet penetration characteristics and trajectories, a two-component PIV investigation was carried out at the centreplane of the flat plate. The transverse jet was seeded and regulated. PIV results provided very useful information regarding the jet mixing and penetration behaviour. Raw PIV analysis was conducted to determine the jet penetration boundaries, whereas instantaneous velocity vectors showed the oscillating nature of the interaction. Ensemble-averaged streamwise and transverse velocity contours revealed the mean flow structures. The locus of maximum velocity is a curved line and its height from the wall is initially decreasing with the streamwise distance in the nearfield and afterwards it starts to increase in the farfield. The barrel shocks and the Mach disc forming the jet boundary were visualised/quantified for the first time in open literature using PIV measurement technique. The streamwise and vertical turbulence components evolved differently throughout the interaction. The

turbulent fluctuations were found to be highly anisotropic, with the streamwise component dominating in the near field. Maximum turbulence occurred above the Mach disc due to the presence of the shear layer and at the intersection of the windward side of the barrel shock and bow shock. Quadrant decomposition addressed uneven organisation of turbulence above the Mach disc, where streamwise fluctuations were more prominent than transverse fluctuations in opposite sign and in the jet core downstream, where transverse fluctuations were more prominent than streamwise fluctuations in opposite sign. As jet to free stream momentum flux ratio,  $J$ , is increased the extent of the local jet boundary composed of the barrel shocks and Mach disc, and the extent of jet spreading were increasing.

## References

- [1] Spaid F. W. and Zukoski E. E.: Study of the Interaction of Gaseous Jets from Transverse Slots with Supersonic External Flows. AIAA J. Vol. 6, No. 2, 205–212, 1968
- [2] Spaid F. W.: Two-Dimensional Jet Interaction Studies at Large Values of Reynolds and Mach Numbers. AIAA J. Vol. 13, No. 11, 1430–1434, 1974
- [3] Schetz J. A. and Billig F. S.: Penetration of Gaseous Jets Injected into a Supersonic Stream. J. of Spacecraft and Rockets Vol. 3, No. 11, 1658–1665, 1966
- [4] Parthasarathy K. and Zakkay V.: An Experimental Investigation of Turbulent Slot Injection at Mach 6. AIAA J. Vol. 8, No. 7, 1302–1307, 1969
- [5] Hawk N. E. and Amick J. L.: Two-Dimensional Secondary Jet Interaction with a Supersonic Stream. AIAA J. Vol. 5, No. 4, 555–660, 1967
- [6] Werle M.J., Driftmyer R.T., and Shaffer D.G.: Jet-Interaction-Induced Separation: The Two-Dimensional Problem. AIAA J., Vol. 10, No. 2, 188–193, 1971

- [7] Kontis K. and Stollery J. L.: Control Effectiveness of a Jet Slender Body Combination at Hypersonic Speeds. J. of Spacecraft and Rockets, Vol. 34, No. 6, 1997
- [8] Gruber M. R., Nejad A. S., Chen T. H., and Dutton J. C.: Mixing and Penetration Studies of Sonic Jets in a Mach 2 Freestream. J. of Propulsion and Power, Vol. 11, No. 2, 1995, pp. 315-323
- [9] Gruber M. R., Nejad A. S., Chen T. H., and Dutton J. C.: Transverse Injection from Circular and Elliptic Nozzles into a Supersonic Crossflow. J. of Propulsion and Power Vol. 16, No. 3, pp. 449-457, 2000
- [10] Ben-Yakar A.: Experimental Investigation of Mixing and Ignition of Transverse Jets in Supersonic Crossflows. Ph.D. Thesis, Department of Mechanical Engineering, Stanford University, CA, USA, 2001
- [11] Schetz J. A., Kush E. A., and Joshi P. B.: Wave Phenomena in Liquid Jet Breakup in a Supersonic Crossflow. AIAA J. Vol. 18 No.7, 1980
- [12] Santiago J. G. and Dutton J. C.: Crossflow Vortices of a Jet Injected into a Supersonic Crossflow. AIAA J., Vol. 35, No. 5, 1997
- [13] Haven B. A. and Kurosaka M.: Kidney and Anti-Kidney Vortices in Cross-flow Jets. J. Fluid Mech. 352, 1997
- [14] Fric, T. F. and Roshko A.: Vortical Structure in the Wake of a Transverse Jet. J. Fluid Mech., 279, 1994.
- [15] Perurena B. J., Asma C. O., Theunissen R., and Chazot O.: Experimental Investigation of Liquid Jet Injection into Mach 6 Hypersonic Crossflow. Exp. in fluids, Vol. 46, No. 3, 403-417, 2009
- [16] Erdem E., Saravanan, Kontis K.: Penetration and Mixing Characteristics of Air, Carbon Dioxide and Helium Jets in Mach 5 Cross Flow, Sensors Journal, 2014



- [17] Haertig J., Havermann M., and Rey C.: Particle Image Velocimetry in  
680 Mach 3.5 and 4.5 Shock-Tunnel Flows. AIAA Journal, 2002; 40: 1056
- [18] Schrijer F., Scarano F., and van Oudheusden B. W.: Application of PIV  
in a Mach 7 Double-Ramp Flow. Exp. in Fluids 41, 2006
- [19] Scarano F.: Overview of PIV in Supersonic Flows. Schroeder A., Willert  
C. E. (Eds.): Particle Image Velocimetry, Topics Appl. Physics 112, 2008
- [20] Huang W.: Transverse Jet in Supersonic Crossflows. Aerospace Science and  
685 Technology, Vol. 50, 2016
- [21] Huh J. and Lee S.: Numerical Study on Lateral Jet Interaction in Super-  
sonic Crossflows. Aerospace Science and Technology, Vol. 80, 2018
- [22] Zhao M., Bian Y., Li Q., and Ye T.: Large Eddy Simulation of Transverse  
690 Single/Double jet in Supersonic Crossflow. Aerospace Science and Technology,  
Vol. 89, 2019
- [23] Williams N. J., Moeller T. M. and Thompson R. J.: Numerical Simula-  
tions of High Frequency Transverse Pulsed Jet Injection into a Supersonic  
Crossflow. Aerospace Science and Technology, Vol. 103, 2020
- [24] Liu Y., Sun M. B., Yang Y. X., Liang C. H., and Wang H. B.: Turbulent  
695 Boundary Layer Subjected to a Sonic Transverse Jet in a Supersonic Flow.  
Aerospace Science and Technology, Vol. 104, 2020
- [25] Miller W. A., Medwell P. R., Doolan C. J., and Kim M: Transient Interaction  
between a Reaction Control Jet and a Hypersonic Crossflow. Phys. Fluids 30,  
700 046102, 2018
- [26] Erdem E: Active Flow Control Studies at Mach 5: Measurement and Com-  
putation. University of Manchester, 2011
- [27] V. Sharma, V. Eswarana, and D. Chakraborty: Effect of Fuel-Jet Injec-  
tion Angle Variation on the Overall Performance of a SCRAMJET Engine.  
705 Aerospace Science and Technology, Vol. 100, 2020

- [28] V. Sharma, V. Eswarana, and D. Chakraborty: Effect of Location of a Transverse Sonic Jet on Shock Augmented Mixing in a SCRAMJET Engine. Aerospace Science and Technology, Vol. 96, 2020
- [29] Z. Dua, W.Huang, L. Yan, and M. Dong: Impacts of Jet Angle and Jet-  
710 to-Crossflow Pressure Ratio on the Mixing Augmentation Mechanism in a Scramjet Engine. Aerospace Science and Technology, Vol. 94, 2019
- [30] N. J. Williams, T. M. Moeller, and R. J. Thompson: Numerical Simulations of High Frequency Transverse Pulsed Jet Injection into a Supersonic Crossflow. Aerospace Science and Technology, Volume 103, August 2020.
- [31] Erdem E. and Kontis K.: Numerical and Experimental Investigation of  
715 Transverse Injection Flows. J. Shock Waves, DOI 10.1007/s00193-010-0247-1, 2010
- [32] Erdem E., Kontis K. and Yang L.: Steady Energy Deposition at Mach 5 for Drag Reduction. J. Shock Waves, DOI 10.1007/s00193-012-0405-8, 2012
- [33] Melling A.: Tracer Particles and Seeding for Particle Image Velocimetry.  
720 Meas. Science and Technology, Vol. 8, 1997
- [34] Samimy M. and Lele S. K.: Motion of Particles with Inertia in a Compressible Free Shear Layer. Phys. of Fluids, Vol.3, 1991
- [35] LaVision GmbH: Flow Master Manual. 2010
- [36] Moffat R. J.: Describing the Uncertainties in Experimental Results. Exp.  
725 Thermal Fluid Sci. 1(1), 3–17 (1988)
- [37] Arnal D. and Delery J.: Laminar-Turbulent Transition and Shock Wave/Boundary Layer Interaction. EN-AVT-116-04, 2004
- [38] Cassel L. A.: Applying Jet Interaction Technology. J. of Spacecraft and  
730 Rockets, Vol. 40, No. 4, 523–537, 2003

- [39] Papamoschou D. and Roshko A.: The Compressible Turbulent Shear Layer: An Experimental Study. *J. Fluid Mech.* 197, 453, 1988
- [40] Havermann M., Haertig J., Rey C., and George A.: PIV Measurements in Shock Tunnels and Shock Tubes. Schroeder A., Willert C. E.: Particle Image Velocimetry, *Topics Appl. Physics* 112, 735
- [41] Sun Z., Schrijer F., Scarano F., and van Oudheusden B. W.: The Three-Dimensional Flow Organization Past a Micro-Ramp in a Supersonic Boundary Layer. *Phys. Fluids*, 24, 055105 (2012)
- [42] Ragni D., Schrijer F., van Oudheusden B. W., and Scarano F.: Particle Tracer Response Across Shocks Measured by PIV. *Exp. Fluids*, 50, 2011 740
- [43] Viti V., Neel R., and Schetz, J. A.: Detailed Flow Physics of the Supersonic Jet Interaction Flow Field. *Phys. Fluids* 21, 2009